



Quantification and simulation of thermal decomposition reactions of Li-ion battery materials by simultaneous thermal analysis coupled with gas analysis

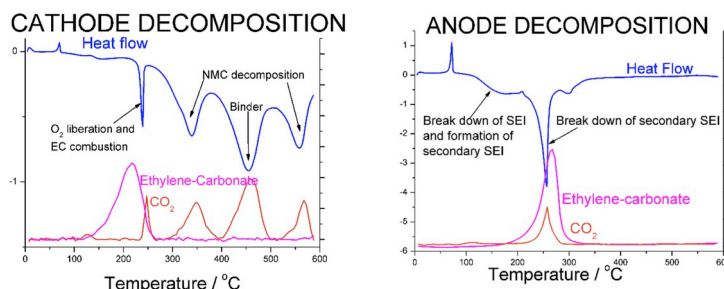
Akos Kriston^{*}, Ibtissam Adanouj, Vanesa Ruiz, Andreas Pfrang

European Commission, Joint Research Centre (JRC), Westerduinweg 3, NL-1755, LE Petten, the Netherlands

HIGHLIGHTS

- Thermal decomposition of active materials in Li-ion cell is analyzed.
- Simultaneous Thermal Analysis coupled with gas analysis is used to identify the processes.
- Double break down mechanism is proposed for graphite decomposition.
- NMC decomposition coupled with electrolyte combustion are assumed.
- Mean and the variance of thermal trip-lets have been calculated and heat flow is simulated.

GRAPHICAL ABSTRACT



ARTICLE INFO

Keywords:

Li-ion
Battery
Thermal runaway
Safety
Simultaneous thermal analysis
Simulation

ABSTRACT

Differential Scanning Calorimetry (DSC) and Thermal Gravimetry (TGA) combined with gas analysis are used to identify the main decomposition processes and to develop reaction kinetic models for thermal runaway modelling of Graphite – Lithium Nickel–Manganese–Cobalt-Oxide (NMC 111) cells. Heating rates of 5, 10 and 15 °C min⁻¹ with multiple replications are performed to determine the frequency factor, activation energy and the heat of reaction of the different sub-processes. It is found that both the anode and cathode decompose in multiple parallel and consecutive reactions between 5 °C and 600 °C. A double breakdown mechanism of the protecting Solid Electrolyte Interface (SEI) is suggested to describe the anode decomposition reactions. For the cathode, decomposition and evaporation of ethylene carbonate (EC), decomposition of NMC with the liberation of oxygen, combustion of EC with the liberated oxygen, decomposition of binder, decomposition of EC and combustion of carbon additive reactions are identified and modelled. The proposed model can be used to simulate thermal runaway initiation methods in a realistic way.

1. Introduction

Various standards and regulations include tests [1] for the characterization of safety performance of batteries during non-normal

circumstances (e.g. overcharge, external short circuit, crash) [2]. However, testing thermal propagation (TP) of batteries caused by internal short circuit during normal operation (e.g. Boeing 787 incident [3–6]) is still in the forefront of research and discussions [7]. Standards

^{*} Corresponding author.

E-mail address: akos.kriston@ec.europa.eu (A. Kriston).

<https://doi.org/10.1016/j.jpowsour.2019.226774>

Received 25 April 2019; Received in revised form 15 June 2019; Accepted 18 June 2019

Available online 1 July 2019

0378-7753/© 2019 The Authors. Published by Elsevier B.V. This is an open access article under the CC BY license (<http://creativecommons.org/licenses/by/4.0/>).

and regulations have identified several possible methods [1,8–10] but there is no common agreement which one can be used for a fit-for-purpose regulation. The difficulty stems from the fact that the determination of suitable testing parameter combinations by experimentation requires an unmanageable number of iterations. Alternatively, simulation can be used [11] to design and optimize an initiation method. However, use of a 3D model can be prohibitively computational expensive to assess the effect of all combinations of possible parameters on thermal runaway.

Our overall goal therefore is to develop a simplified model, able to assess the most significant parameters for triggering thermal runaway (TR) induced by internal short circuit and thereby, to narrow down the testing needs. However, published thermal decomposition models found are not fully suitable for this purpose. Consequently, as a first step, thermal data together with measurement uncertainty is determined from Differential Scanning Calorimetry (DSC), Thermal Gravimetric Analysis (TGA) and gas analysis. From these, an approximate kinetic model is developed, which is able to mimic the dynamics of TR in a realistic way. In a second (follow up) paper, this model is used to simulate TR and to calculate the probability of thermal runaway as a function of the parameters of a triggering method.

In the next sub-sections, first a summary of experimental methods and their main conditions are given. Then, the key decomposition reactions are listed for graphite, NMC and electrolyte. Finally, different kinetic models, developed for the decomposition reactions, are summarized.

1.1. Test methods and conditions

Accelerated Rate Calorimetry (ARC), Differential Scanning Calorimetry (DSC), Differential Thermal Analysis (DTA), Thermal Gravimetric Analysis (TGA) coupled with gas analysis are the commonly used methods for the characterization of thermal decomposition reactions of Li-ion batteries and materials. McNeil and Dahn [12] compared ARC and DSC measurements and found that they are equivalent, however ARC is more sensitive to determine the reaction order, while DSC is more precise to determine the so-called thermal triplets (activation energy, frequency factor and heat of reaction). Furthermore, ARC is unfit to detect endothermic reactions [13]. Simultaneous Thermal Analysis (STA), which consists of DSC and TGA, is also performed [14] and there, more information can be retrieved.

The sample crucible is usually sealed for ARC and DSC tests [15,16]. Obviously for TGA and STA tests, the crucible cannot be closed [17]. For open systems, the size of the opening in the crucible is of utmost importance. Watanabe and Yamaki [18] investigated the effect of the size of the opening and showed that if the opening is small, the DTA signal is similar to tests with a sealed crucible. However, the DTA signal obtained by crucibles with large opening is considerably suppressed. The size of the opening also influences gas evolution and mass loss [18]. In an open system, the solvent(s) evaporate(s) earlier, which may result in different reactions from those occurring in a closed or half closed system. Pressure and concentration of the substances may influence reaction rates, which in turn, may result in different products and yields, consequently, different heat production. It is difficult to determine which experimental setup – open or closed crucible – is the most appropriate for simulating a realistic scenario, because all batteries vent under certain but different abusive conditions.

At least, three different sample preparation methods have been used in literature for thermal analysis of electrodes: a) washing followed by drying, b) drying (without prior washing) followed by adding electrolyte, c) drying only (without prior washing and without adding electrolyte). Zhuang used Attenuated Total Reflection Fourier-transform Infrared Spectroscopy (ATR FTIR) to identify the components of Solid Electrolyte Interphase (SEI) and found that washing modifies SEI considerably [19], however in this case, the effect of the electrolyte on the decomposition reaction and heat of active materials can be studied

[17]. MacNeil et al. [12] showed that electrode drying or exposure to the glove box (GB) atmosphere alters the decomposition heat of Li-Cobalt-Oxide (LCO). There is no general agreement on the optimal drying time, furthermore, there is no general agreement about the amount of the extra added electrolyte to the crucible. Often, the amount is not mentioned in reported experiments. Xuning et al. [20] found in their review that the amount of added electrolyte is crucial for DSC and ARC investigations and requires further study.

Because the difference in the purpose of the experiment may justify the selection of different experimental and sample preparation techniques, the comparability of the outcome of different experiments is not straightforward. It is also crucial to understand which approach is the most representative for a real thermal runaway scenario.

In this work, as gas analysis is used, we have chosen an open system, but the hole of the crucible is made as small as possible (see section 2.3). No washing and no extra electrolyte are applied to minimize SEI modification. The harvested samples are dried for 2 h before the STA study to reach a stable initial mass for TGA and to suppress the effect of endothermic evaporation heat on the measureable heat release.

1.2. Graphite anode reactions

Depending on the studied material and the experimental conditions, several decomposition processes have been identified in the literature. Table 1 summarizes, comparable to our experimental conditions (see section 2.3), the decomposition processes, grouping them by components and evolved gases. Further descriptions about the reactions are given in supplementary materials.

The reaction mechanism, as reviewed by Spotnitz et al. [22], starts with the decomposition of the metastable SEI components to more stable

Table 1

Identified decomposition reactions at the anode at elevated temperature. R is a low-molecular-weight alkyl group. *p*-SEI stands for the primary SEI developed during cycling and *s*-SEI for secondary SEI, which may form at elevated temperature at the beginning of TR. Ethylene carbonate (EC) and dimethyl carbonate (DMC) are the solvents used in the electrode. Carboxymethyl cellulose (CMC) is the binder material.

#	Initial component	Evolved gases	Reaction	Ref.
1	<i>p</i> -SEI	CO ₂	(R-OCO ₂ Li) ₂ → (R-O-Li) ₂ + 2CO _{2(g)}	[17]
2	<i>p</i> -SEI	CO ₂	ROCO ₂ Li + HF _(g) → ROH _(s) + CO _{2(g)} + LiF _(s) 2 ROCO ₂ Li + H ₂ O _(g) → 2 ROH _(s) + Li ₂ CO _{3(s)} + CO _{2(g)}	[21]
3	<i>p</i> -SEI	CO ₂ , O ₂ , ethylene	(CH ₂ OCO ₂ Li) ₂ → Li ₂ CO _{3(s)} + C ₂ H _{4(g)} + CO _{2(g)} + 1/2 O _{2(g)}	[22–24]
4	<i>p</i> -SEI + Li	ethylene	(CH ₂ OCO ₂ Li) ₂ + 2Li → 2 Li ₂ CO _{3(s)} + C ₂ H _{4(g)}	[22–24]
5	<i>p</i> -SEI + Li	No gases	(CH ₂ OCO ₂ Li) ₂ + 2Li → (COOLi) _{2(s)} + (CH ₂ OLi) _{2(s)} 2CH ₃ OCO ₂ Li + 2Li → (COOLi) _{2(s)} + 2 CH ₃ OLi _(s)	[25,26]
6	s-SEI + LiPF₆	POF ₃ or No gases	(R-O-Li) ₂ + PF ₅ (or LiPF ₆) → (2) LiF + Li-O-R-F + POF _{3(g)} POF _{3(g)} + 2xLi → Li _x POF _{3-x(s)} + xLiF _(s)	[13,17]
7	<i>s</i> -SEI + LiPF ₆	CO ₂	LiPF ₆ + 2Li ₂ CO ₃ → 2CO ₂ + 4LiF + F ₂ PO ₂ Li	[27]
8	Li + Solvent	CO ₂	2 Li(C ₆) + 2 EC → Li-O-(CH ₂) ₄ -O-Li _(s) + 2 CO _{2(g)}	[17]
9	Li + Solvent (EC)	ethylene	C ₃ H ₄ O ₃ + 2Li(C ₆) → Li ₂ CO _{3(s)} + C ₂ H _{4(g)}	[22]
10	Li + solvent (DMC)	propylene	C ₃ H ₆ O ₃ + 2Li(C ₆) → Li ₂ CO _{3(s)} + C ₂ H _{6(g)}	[22]
11	CMC binder	CO ₂ , H ₂ O	CMC → levoglucosan _(s) + CO _{2(g)} + H ₂ O _(g)	[28]
12	CMC + Li	H ₂	CMC-OH + Li ⁺ + e ⁻ → CMC-Oli _(s) + 1/2 H _{2(g)}	[21]

inorganic ones, such as reaction 4 in Table 1 with exothermic heat release from about 100 °C. When the SEI decomposes, EC (ethylene carbonate) reaches the surface of the graphite and starts to react with the intercalated Li according to reactions 8–9. These reactions are highly exothermic, but create further inorganic protective layer, which finally slows down the process. Richard et al. [23,29,30] proposed a diffusion type kinetics, where the diffusion layer continuously thickens meanwhile heating up the cell:

$$R_{SEI} = \frac{dx_{SEI}}{dt} = -A_{SEI}x_{SEI}\exp\left(-\frac{E_{SEI}}{k_B T}\right) \quad 1$$

$$R_{LiC} = \frac{dx_{LiC}}{dt} = -A_{LiC}x_{LiC}\exp\left(-\frac{E_{LiC}}{k_B T}\right)\exp\left(-\frac{t_{SEI}}{t_{SEI,Ref}}\right) \quad 2$$

$$\frac{dt_{SEI}}{dt} = A_{LiC}x_{LiC}\exp\left(-\frac{E_{LiC}}{k_B T}\right)\exp\left(-\frac{t_{SEI}}{t_{SEI,Ref}}\right) \quad 3$$

where A_i is the frequency factor (s^{-1}), E_i is the activation energy (J), x_i is the dimensionless concentration and t_i is the thickness of the diffusion film with $i = SEI$ and LiC (lithiated graphite), respectively. k_B is the Boltzman constant ($J K^{-1}$) and T is the temperature (K) and R_i is the reaction rate (s^{-1}). This model [22,23,29–31] has been used for several years, recently in Refs. [11,32], for modelling thermal runaway, despite Richard et al. [23,29,30] mentioned that their model was better suited to capture the onset of TR.

Feng and Xuning et al. [20,33,34] proposed a modification to Richard's equation [23,29], where the SEI decomposes according to Eq. (1) and forms simultaneously according to Eq. (3). A gain factor, K was introduced to take into account the newly formed SEI [20].

$$\frac{dx_{SEI}}{dt} = -A_{SEI}x_{SEI}\exp\left(-\frac{E_{SEI,Li}}{k_B T}\right) + KA_{LiC}x_{LiC}\exp\left(-\frac{E_{LiC}}{k_B T}\right)\exp\left(-\frac{t_{SEI}}{t_{SEI,Ref}}\right) \quad 1a$$

The gain factor K was determined by fitting and the best fit was obtained for $K = 5$ [20,33,34]. The heat of reaction was assumed to be the same for the newly formed SEI, i.e. there is no distinction between the primary and secondary SEI.

Other authors proposed the following mechanism [14,24,35]: the primary SEI (p-SEI) layer breaks down from around 100 °C (e.g. reaction 1–5 in Table 1), then Li starts to react with the electrolyte and builds up a secondary SEI layer (s-SEI) (e.g. reaction 5 in Table 1 producing metastable compounds). The s-SEI is stable enough to protect further EC-Li reactions. However, with increasing temperature, the metastable part of the secondary SEI layer breaks down together with imminent EC-Li reaction resulting in a sharp exothermic peak around 250 °C (e.g. reaction 6–10 in Table 1). No kinetic expression has been proposed yet, therefore, in this work, an approximate kinetic expression is formulated to be able to model TR in the full temperature range.

1.3. NMC cathode reactions

The reviewed decomposition reaction of NMC (111) is summarized in Table 2. Further details about the reactions are given in the supplementary materials.

The first kinetic model for LCO electrodes has been developed by MacNeil et al. [12] and Hatchard et al. [30], which is used for several simulation studies [11,20,31,32]. An autocatalytic reaction mechanism was proposed and the reaction parameters were determined by ARC and DSC experiments. Later, the same autocatalytic reaction mechanism was suggested and used for other cathode materials, such as LCO, NMC(111), NCA, LMO, LFP, by Peng et al. [38]. It is common to all models that only one decomposition reaction is taken into account, despite the electrode containing binder and the fact that oxygen is released from NMC(111) in a multistep process according to Li et al. [39].

Table 2

Identified decomposition reactions of NMC(111) de-lithiated cathode.

#	Initial components	Evolved gases	Reaction	Ref.
13	NMC	O ₂	$Li_xNi_{1/3}Co_{1/3}Mn_{1/3}O_2 \rightarrow Li_xNi_{1/3}Co_{1/3}Mn_{1/3}O_{2-y(s)} + 1/2yO_{2(g)}$	[31, 36]
14	C (additive)	CO ₂	$C + O_2 \rightarrow CO_{2(g)}$	
15	NMC, HF (from LiPF ₆)	H ₂ O	$Li_{(1-x)}Ni_{1/3}Mn_{1/3}Co_{1/3}O_2 + 4(1-x)HF \rightarrow (3x-1)Ni_{1/3}Mn_{1/3}Co_{1/3}O_{2(s)} + 2(1-x)H_2O_{(g)} + (1-x)MnF_{2(s)} + 2(1-x)LiF_{(s)} + 2(1-x)Ni_{0.5}Co_{0.5}O_2$	[37]

1.4. Electrolyte reactions

While Campion et al. [40] and Wang et al. [41] suggested that EC reacts with LiPF₆ salt at around 200–230 °C, Yang et al. [42] did not find evidence for that reaction. The difference might originate from the different measurement conditions. Campion et al. [40] and Wang et al. [41] used sealed crucibles, where the reactive decomposition product of LiPF₆ remained near the EC, therefore they were able to react. If TGA and online gas detection were applied, such as by Yang et al. [42], PF₅ or EC was released from the crucible before they could react. Therefore, their reaction was suppressed or completely avoided. Consequently, depending on whether venting happens, the dominating decomposition reactions can be different which in turn may make the comparison of realistic scenarios to laboratory measurements more complicated.

2. Experimental

Freshly assembled, cycled and fully charged materials were used for all STA measurements with subsequent evolved gas analyses.

2.1. Sample materials

Graphite (Gr), NMC (111), binders as pristine materials and the 18 mm discs electrodes made of the same pristine materials were supplied by Customcells (Germany). Further details of the materials are given in supplementary materials.

2.2. Electrochemical tests and preparation for thermal analysis

The protocol for adjusting the SOC consisted of a constant current (CC) charge at C/20 rate up to a cut-off voltage of 4.2 V, followed by a resting period of 1 h (OCV), and a CC discharging at a C/20-rate to a cut-off voltage of 3 V. This cycling process was repeated twice in total, followed by charging to cut-off voltage of 4.2 V. This voltage threshold is considered full charge. The actual lithiation percentage of graphite and de-lithiation percentage of each NMC were calculated from the actual loading and rated capacity (further details about the testing conditions can be found in supplementary materials).

After SOC adjustment, the electrochemical cell was transferred to the glove box for disassembly. The anode and cathode sample were then weighed and afterwards dried in the vacuum antechamber of the glove box at approximately 1 mbar for 2 h at room temperature. Under these conditions, DMC solvent is expected to evaporate fully (due to its low boiling point of 90 °C at 760 mm Hg [43]), whereas EC solvent, with a boiling point of 246.7 °C at 760 mmHg [44], is expected to mainly remain.

Following the drying step, the electrode surface is carefully scratched by using a tweezer and spatula, in order to remove the active material from the current collector. The harvested material is further analyzed to characterize its thermal properties and the evolved gas during heating.

2.3. Simultaneous thermal analysis

DSC/TGA tests were carried out using a STA 449F3 – Jupiter® Simultaneous Thermal Analysis, instrument (Netzsch, Germany) with a silver furnace and a TGA-DSC sample carrier for evaluating the thermal behaviour of the collected materials. As shown in Fig. 1, this apparatus is located inside an Ar-filled glove box (MBraun MB 200B, H₂O < 0.1 ppm; O₂ < 0.1 ppm), which was connected to the glove box used for sample preparation. Therefore, the samples remain constantly under inert atmosphere and exposure to air is excluded. STA was operated using helium as a carrier gas for both the purge of the sample compartment (flow rate of 50 ml min⁻¹) and as protective gas (flow rate of 20 ml min⁻¹). After placing the crucible inside the sample chamber, the chamber was carefully evacuated and refilled with helium 2 times to flush argon originating from glove box atmosphere.

In the glove box, the harvested anode or cathode material is loaded in a sealed aluminium crucible with laser-pierced lid (opening 5 µm diameter) for each Differential Scanning Calorimetry/Thermogravimetric Analysis (DSC/TGA) test. No extra electrolyte was added to the crucible. The actual weight of the sample and the crucible has been measured before placing in the STA.

All measurements were carried out from 5 °C to 590 °C starting with an isothermal phase of 20 min at 5 °C then continuing with heating rates of 5, 10 and 15 °C min⁻¹ with STC control. At the end of the dynamic heating phase, an isothermal stage of 10 min at 590 °C was applied before cooling to room temperature. The measurements were repeated at least 3 times for each heating rate. The TG and DSC data were analyzed by Netzsch Proteus® software.

2.4. Analysis of evolved gases

Gas analysis was not performed on all samples. When it was used, the flow rate of the process gas in the STA was increased to 100 ml min⁻¹. This higher flow rate was necessary to be able to split the gases between the two pieces of analytical equipment. The sensitivity to gases released during the decomposition at smaller quantity can be increased by increasing the amount of material but in this case, the accuracy of heat flow measurement may be reduced. In the current experiments, however the sensitivity for the main reported gas compounds was satisfactory and the amount of sample was not increased.

The gases released during thermal decomposition were constantly monitored using GC-MS (Agilent 7820A gas chromatograph equipped with an Agilent 5977E quadrupole MS) and FTIR (Bruker Vertex 70 V Fourier Transform Infrared spectrometer), both coupled with STA equipment via heated transfer lines (150 °C) (Fig. 1). The following parameters for the GC-MS were used: column type: HP-PLOT-U (Agilent, 35 m length, 0.32 mm internal diameter, 0.01 mm film thickness, max. temperature 180 °C), split ratio 10:1; helium flow rate: 1.5 ml min⁻¹;

temperature program: 100 °C (60 min), 10 °C min⁻¹ up to 150 °C (10 min) and 10 °C min⁻¹ to 100 °C. At the beginning and the end of the HP-PLOT-U column, 2 m of trap columns (Agilent, 0.32 mm siloxane stationary phase) were attached to protect the main column from HF and to protect the MS from the possibly detached particles, respectively. The MS detector was used in scan mode. Composition of evolved species was determined using Netzsch GC-MSD Data Analysis software.

The 10 cm path IR gas-cell was heated to 200 °C. Together with the liquid nitrogen cooled detector, they were placed in the TG-IR Box (Netzsch, Germany) which was purged with Ar during the measurement. Even though the TG-IR box and the Vertex V70 were placed as close as possible to each other (<1 cm), the IR beam passed through a short non-evacuated path and might collect the signals of CO₂ and H₂O from the atmosphere. This effect was compensated by background correction after the measurement. The FTIR spectra were collected in absorbance mode from the wavelength range of 500–4500 cm⁻¹ with 4 cm⁻¹ spectral resolution and 18 spectra were collected. OPUS software version 7.2 (Bruker, Germany) was used to process the FTIR spectral data. The qualitative identification of gas compounds of MS spectra and FTIR graphs was performed based on online NIST Standard Reference Database 35 (a NIST/EPA Gas-Phase Infrared library).

JMP software (SAS, USA) was used to calculate activation energy and frequency factor. Matlab 2018a (Mathworks, USA) was used to simulate DSC curves.

3. Results and discussion

The decompositions of the anode, cathode and the electrolyte are discussed separately. For establishment of all decomposition reactions, the following steps are taken:

- Identification of possible reaction mechanisms from Tables 1,2 and 3.
- Thermal analysis for the identified most important DSC peaks
- Calculation of thermal parameters: heat of reaction, frequency factor, activation energy and their uncertainty
- Simulation of the kinetic reactions and heat flow

The main goal of the analysis is to find a model that describes the heat generation resulting from anode, cathode and electrolyte decomposition for the used chemistry and electrode design in the temperature range 20–590 °C.

3.1. Electrochemical characterization of coin cells

Table 4 shows the investigated cells' capacities and the calculated lithiation, delithiation levels for the Gr anode and NMC (111) cathode, respectively. According to the manufacturer, the anode electrode has

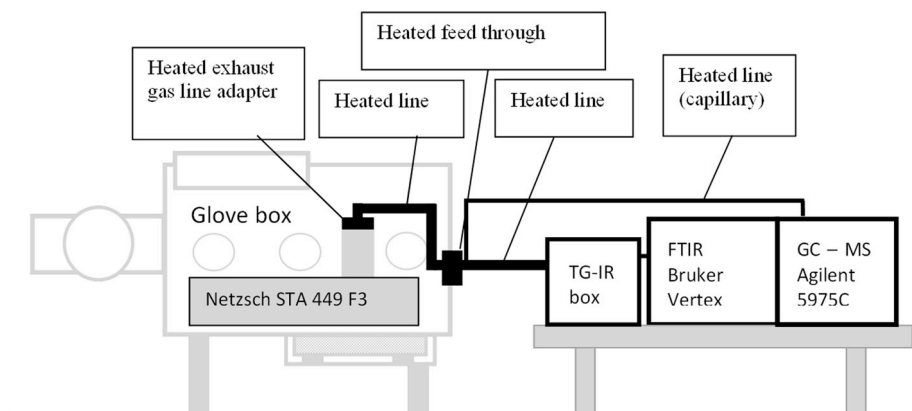


Fig. 1. The set-up of the coupled measurement system.

Table 3
Identified decomposition reactions of electrolyte.

#	Initial components	Evolved gases	Reaction	Ref.
16	C ₃ H ₄ O ₃	CO ₂ , H ₂ O	C ₃ H ₄ O ₃ + 2.5 O ₂ → 3 CO _{2(g)} + 2H ₂ O _(g) C ₃ H ₄ O ₃ + 2 O _{2(g)} → 2 CO _{2(g)} + CO _(g) + 2H ₂ O _(g)	[41]
17	LiPF ₆	HF, PF ₅	LiPF ₆ → LiF _(s) + PF _{5(g)}	[42]
18	C ₃ H ₄ O ₃	C ₃ H ₄ O ₃	EC evaporation	[42]
19	C ₃ H ₄ O ₃ + LiPF ₆	CO ₂	C ₃ H ₄ O ₃ + PF ₅ → CO _{2(g)} + Fluoro-Polyethylene Oxide (PEO) _(s)	[40, 41]
20	C ₃ H ₄ O ₃	CO ₂ , H ₂ O	C ₃ H ₄ O ₃ → 3 CO _{2(g)} + 2H ₂ O _(g)	

been designed to have 10% higher capacity than the cathode to avoid Li plating on the graphite anode. According to our measurement, the anode has on average 11% higher capacity than the cathode. It should be noted that the NMC delithiation level in sample #10 and #11 is higher than it is expected by the manufacturer, which is most probably stemming from the variation of composition and non-uniform distribution of active electrode material on the current collector surface. Fig. 2 shows the cycling behaviour of the cell for sample #5 in Table 4. The anode potential in this configuration does not reach 0 V vs. Li, the theoretical maximum lithiation, but stops at around 50 mV vs. Li. Consequently, Li plating is not expected. Furthermore, the minimum delithiation is reached at ca. 400 mV. These narrow limits may have an impact on the SEI formation, but for realistic experimental results, it is important to keep the cycling potential range close to that in real cells.

3.2. Decomposition of lithiated graphite anode

Fig. 3a shows a representative simultaneous thermal analysis result: heat flow (mW/mg), mass loss (wt%), and the relative FTIR intensity of CO₂ (2346 cm⁻¹) and EC (1863 cm⁻¹), obtained for fully charged graphite anode active materials (Sample #5 from Table 4) as a function of the testing temperature from 5 °C to 590 °C at 10 °C min⁻¹ heating rate. The decomposition profile can be split into 4 different regions (shown by Arabic numbers), which are discussed separately in the followings. Roman numbered peaks show the analyzed peaks due to their importance on heat flow.

Fig. 3b and c show the FTIR spectra registered at 110 °C and 250 °C, respectively. The pristine CO₂, ethylene, and water spectra reproduced from NIST are also shown for comparison.

In region 1 below 100 °C, no mass loss or gas formation is detected, however the DSC signal shows a sharp endothermic peak around 70 °C. This peak is far from EC melting (ca. 36 °C) and from DMC evaporation

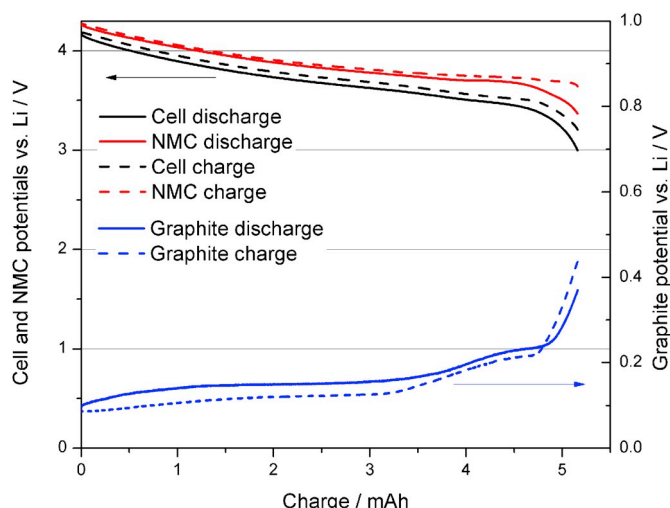


Fig. 2. The 2nd cycle of sample #5 in Table 4 at C/20.

(90 °C) [45]. This endothermic peak can also be found on pristine graphite after contact with the electrolyte without cycling (see Fig. S1a in the supplementary material), therefore it is not considered to be related with the lithiated graphite. The origin of this peak is currently unknown, but some possible causes are discussed in the supplementary materials. This peak's influence on TR is minimal and therefore, neglected from further calculations and analysis.

Region 2 is commonly identified as the breakdown of SEI followed by the reaction of Li with electrolyte according to reactions 3, 4 and 9 in Table 1. However, it is not necessary that SEI decomposes in one-step (further explanation is given in supplementary materials). In our system, no evidence is found for one-step SEI decomposition according to 3, 4, and 9. In the beginning of region 2 at 110 °C, the FTIR spectra in Fig. 3b indicates that mostly CO₂ and water is present in the exhaust gas. Only a small increase of CO₂ is detected at around 100–110 °C, but later its concentration drops (see CO₂ FTIR signal intensity at 2346 cm⁻¹ in Fig. 3a and 3b). A small peak of CO₂ is also detected by the GC-MS (not shown) but no ethylene was found, as it is expected from 3, 4 and 9 in Table 1. The ca. 4% mass loss is negligible compared to the expected mass loss of reactions 3, 4, and 9 (in Table 1). Furthermore, it is mostly correlated with the beginning of EC evaporation, as shown by EC's 1863 cm⁻¹ FTIR peak intensity in Fig. 3a and 3c, which starts at around 150 °C. Neither FTIR spectra (Fig. 3b) nor GC-MS show traces of other gases in region 2. Therefore, the most likely reactions from Table 1 are 1, 2 and 5. While CO₂ release occurs only close to 100 °C, it is plausible that

Table 4

Testing matrix for the STA experiments and the investigated cells' main electrochemical properties. n.a. = cycling file corrupted therefore the SOC calculation was not possible, but STA was performed. *scratched sample lost during preparation. Rated capacity was calculated from the mass loading. The discharge capacity is calculated from the second discharge cycle.

Sample #	Sample Name	Rated capacity/Ah		Measured capacity/Ah	Gr/Lithiation	NMC/Delithiation	Heating rate/°Cmin ⁻¹
		Gr	NMC	Cell		%	
1	NMC-Gr-28	6.09	5.14	5.14	84	99	5
2	NMC-Gr-24	5.81	5.28	5.17	86	95	5
3	NMC-Gr-23	6.02	5.29	5.37	87	99	5
4	NMC-Gr-14	5.96	5.25	n.a.	n.a.	n.a.	5
5	NMC-Gr-30	5.57	5.16	5.11	91	98	10
6*	NMC-Gr-27*	5.50	4.74. *	4.65	84	97*	10
7	NMC-Gr-10	5.94	5.27	5.33	81	92	10
8	NMC-Gr-8	6.04	5.24	5.21	80	92	10
9	NMC-Gr-26	5.98	5.29	5.37	89	100	15
10	NMC-Gr-25	5.93	5.31	5.39	90	101	15
11	NMC-Gr-18	5.98	5.10	5.26	87	102	15
12	NMC-Gr-17	5.87	5.28	5.36	86	96	15
				Average	86	97	
				Std.Dev.	3	3	

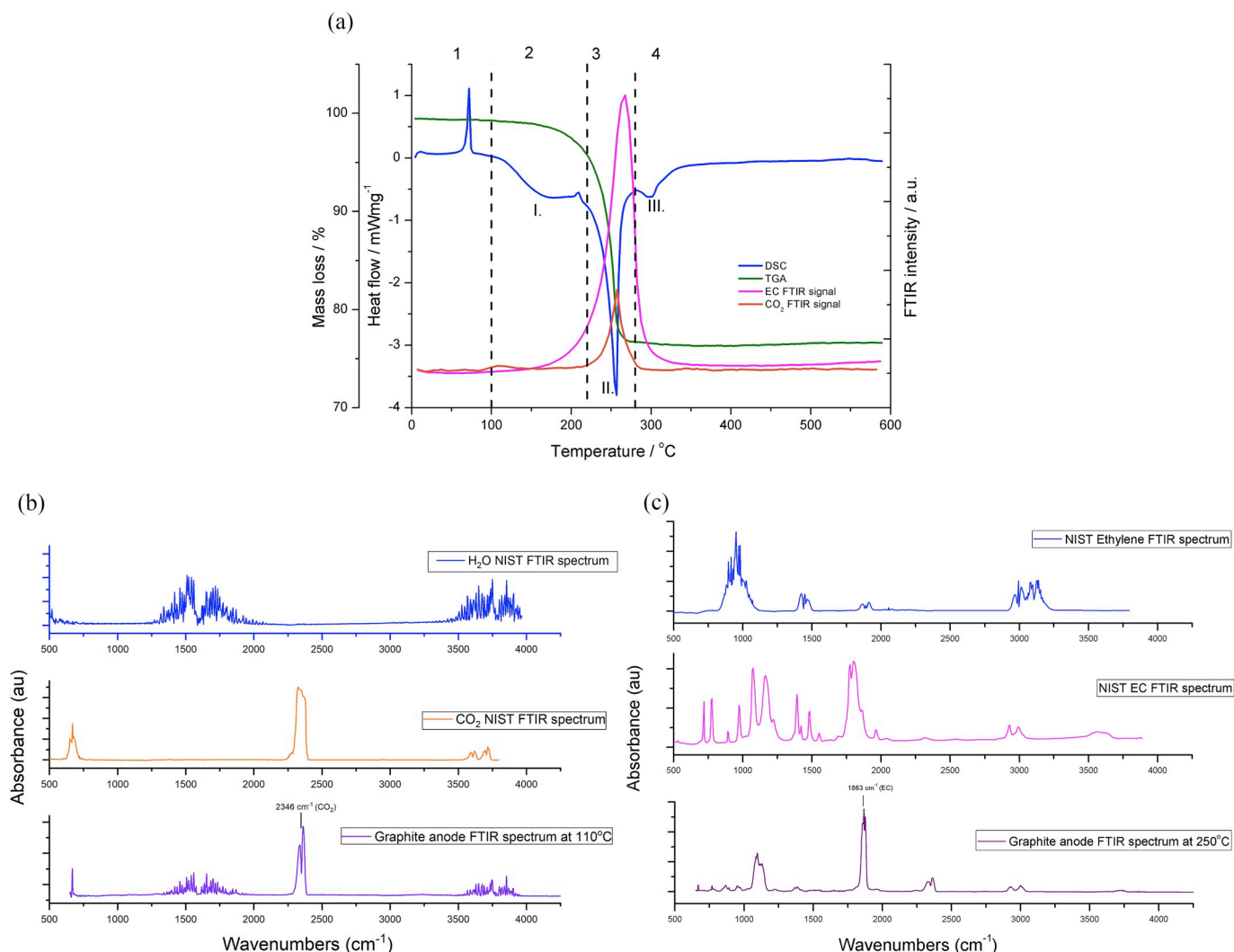


Fig. 3. Simultaneous thermal analysis of lithiated graphite anode #5 at $10^{\circ}\text{C min}^{-1}$ in Table 4 (a), FTIR spectra of the exhaust gas of graphite anode; H_2O (NIST), CO_2 (NIST) at 110°C (b) and graphite anode; ethylene (NIST), EC (NIST) at 250°C (c). The reference spectra have been downloaded from NIST Chemistry WebBook [46]. Arabic numbers represents the regions, which may consist of several peaks. Roman numbers show the significant and modelled peaks.

reaction 2 occurs as traces of water evaporates (Fig. 3b) from the pores or other parts of the system (e.g. crucible). In the current state of research, it is not possible to draw a final conclusion about the origin of this CO_2 peak.

Shortly after or in parallel with the CO_2 peak, a mild heat generation starts and continues after the broad exothermic peak around 150°C – 170°C , identified as peak I. This mild heat generation, with the absence of major mass loss and gas formation, may also indicate that the SEI does not disintegrate but continuously thickens or changes its composition. Reaction 2 in Table 1, which is supposed to happen around 100°C , may render the SEI more permeable for Li-ions or for EC but the new or transformed SEI keeps its protective nature. Furthermore, reactions 3, 4 and 9 in Table 1 should be accompanied by mass loss and more gas generation, especially ethylene [22,23,30], which was not found in region 2. Therefore, reaction 1 and 5 might be possible mechanisms of heat generation rather than 3, 4, and 9. Chen et al. [47] demonstrated, by means of XRD, that the content of lithium in graphite decreased gradually during thermal ramping from 110°C to about 230°C as a consequence of the formation of secondary SEI film. Reaction (s) in region 2 should not generate gas but should consume Li. Therefore, reaction 5 is the proposed mechanism rather than the decomposition of SEI followed by immediate Li-electrolyte reaction according to reactions 3 and 4 or SEI decomposition according to reaction 1. It must be noted

that for other systems where the SEI is different, this scheme may be different.

A small endothermic peak around 200°C can be the consequence of the melting of LiPF_6 or of plated Li [48,49] or graphite exfoliation [50]. This reaction has minor impact on TR and will be excluded from further analysis.

Region 3 starts with a sharp exothermic peak, large mass loss and gas evolution (Fig. 3a). The FTIR spectra in Fig. 3c is more complex than that of in region 2 (Fig. 3b) and there are several unidentified peaks, however the most pronounced compounds with the highest match are CO_2 and EC. GC-MS analysis (not shown) shows the presence of ethylene and PF_3 in addition to the characteristic peaks of CO_2 and EC in the FTIR spectra in Fig. 3c. It indicates that in region 3, multiple reactions may occur at the same time: a) decomposition of SEI, b) Li electrolyte reaction (reactions 3, 4, 6, 7, 8 and 9 from Table 1), c) EC decomposition, LiPF_6 decomposition and EC evaporation (Table 3).

The STA of pristine graphite in contact with electrolyte shows (Fig. S1a in supplementary material) that EC evaporation is the fastest among these reactions under these circumstances. Therefore, reactions 16, 17 and 19 in Table 3 are less relevant. The minor CO_2 generation (Fig. S1a in supplementary material) without HF and PF_3 formation, also supports this assumption. Hence CO_2 , ethylene and PF_3 (decomposition product of LiPF_6) most probably originate from the graphite-EC

decomposition (reaction 6 in Table 1). Even though PF_3 is not a primary product of any reactions listed in Table 1–Table 3, it may be formed in the GC columns or in the heated lines.

In region 3, peak II. is most probably the consequence of multiple consecutive and parallel reactions. Perhaps, it is governed by the slowest reaction; however, the measurable reaction heat is the sum of all reactions. Therefore, in spite of the complex scheme, the exothermic DSC peak II. in region 3 still can be approximated by the Kissinger method if the slowest reaction follows Arrhenius kinetic. Without speculating too much about the possible reaction mechanisms, the most important consideration is that the exothermic reactions in region 2 and in region 3 are different. Therefore, the SEI breakdown and Li-electrolyte reactions are not a single reaction mechanism as suggested by Refs. [22,23,30] and they must be modeled by different reaction mechanisms. In this work, we propose and formulate a double-break down mechanism. It must be noted that this is not a general decomposition reaction model and that may be different for other materials or for the same material tested in a different experimental setup. In region 3, the mass loss is mostly due to EC evaporation as that is faster than EC decomposition and combustion (as it is shown in supplementary materials Fig. 1a).

In region 4, smaller, partly overlapping exothermic peaks are visible (see also Fig. 4a). The mass loss and gas production is minimal and

detectable only at $15^\circ\text{C min}^{-1}$ heating rate. Traces of ethylene are found by GC-MS (not shown) together with C_2H_6 , CH_4 , C_3H_6 (at $15^\circ\text{C min}^{-1}$). This region is in the same temperature range where the decomposition of the binder occurs (Fig. S1b in supplementary material). Evidence for the reaction between the electrolyte and CMC binder was found by El Ouatani et al. [51]. The reactivity of CMC towards the electrolyte is most probably due to hydroxyl functional groups in CMC, which take part in the formation of the surface film and may decompose with higher heat of reaction than the binder alone. Since the fraction of binder is less than 2 wt%, its decomposition cannot explain the measured considerable heat generation. Most probably, though, some reaction products of the previous decomposition reactions decompose further here. Zhao et al. [25] found that at 330°C and 430°C the exothermic reaction is caused by the decomposition of two main SEI components, lithium alkyl carbonate and lithium oxalate. The EC evaporated and/or reacted fully, therefore possible reactions can be only 6, 7, 11 and 12 from Table 1 (which does not require EC). However, none of these reactions explains all the found gases or the absence of gases. Nevertheless, the processes in region 4 are different from the processes in the previous regions, however the reaction products from previous regions may affect reactions in region 4.

As the current work's focus is the calculation of an approximate heat

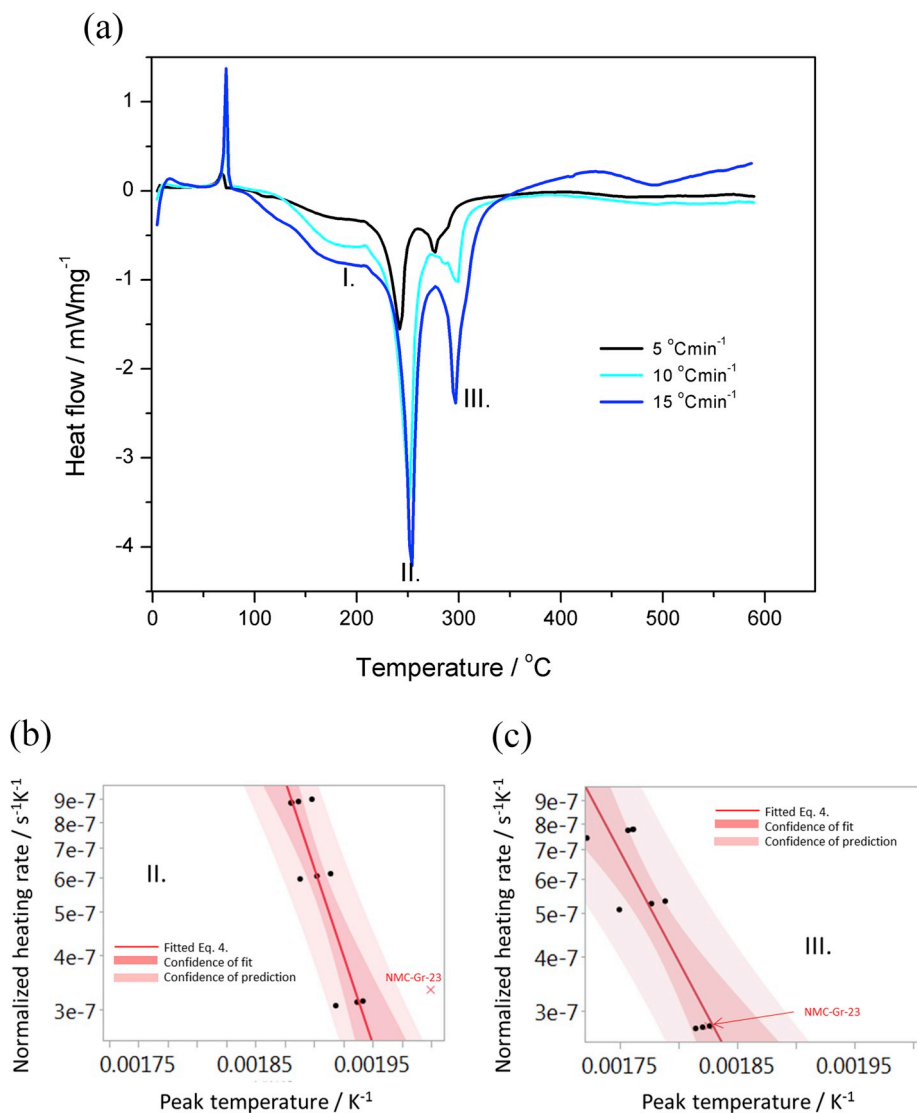


Fig. 4. Heat flow of lithiated anode at heating rates of $5, 10$ and $15^\circ\text{C min}^{-1}$ of samples #2, 6, 9 in Table 4., respectively (a), Kissinger plot of peak II. (b) and Kissinger plot of peak III. (c) for all experiments from Table 4.

generation, Arrhenius type decomposition reaction is considered, in spite of the complex shape of peak III. However, the total heat generation in region 4 was determined and used in the model.

The Kissinger analysis was performed on the DSC curves at three heating rates with several replications (Table 4) by using the following procedure:

The frequency factor and activation energy are calculated by the following equation [52] based on Kissinger's analysis [53].

$$\ln \frac{a}{T_{\max}^2} = \ln \frac{Ak_B}{E} - \frac{E}{k_B T_{\max}} = b - m \frac{1}{T_{\max}} \quad 4$$

where T_{\max} (K) is the temperature at maximum heat release at heating rate a (Ksec^{-1}), k_B is the Boltzmann constant. The activation energy (E) is obtained from the slope (m), and the frequency factor (A) by multiplying b (intercept) and m . The standard error of the activation energy (E) is calculated directly from the standard error of the slope (σ_m). The standard error of the frequency factor is calculated by taking into account the error propagation of the multiplication function

$$\sigma_A = bm \sqrt{\left(\frac{\sigma_m}{m}\right)^2 + \left(\frac{\sigma_b}{b}\right)^2} \quad 5$$

where σ_m is the standard error of the slope and σ_b is the standard error of the intercept of the fitting of Eq. (4).

Fig. 4a shows the anode decomposition DSC curves at 5, 10 and 15 °C min^{-1} heating rates. As the heating rate increases, the intensity of peak II. becomes larger and shifts to higher temperatures, as expected for an Arrhenius-type reaction. Peak III. shows a higher variation in shape than peak II but the most pronounced peak (peak III.) seems to follow an Arrhenius-type behaviour. The shape of peak III. varies probably because it is affected by the reaction products from region 2 and 3.

Peak I., however, shifts to lower temperature with increasing heating rate and becomes narrower; hence, it does not follow an Arrhenius type reaction. Furthermore, at low heating rates, it is hard to identify the peak's maximum because of its broad nature, which makes the Kissinger analysis unreliable in this case.

The Kissinger plots are shown in Fig. 4b and c for peak II. and III., respectively. The temperature at which the maximum depth of the peak is observed, is plotted against the normalized heating rates (5, 10, 15 °C min^{-1}). Since NMC-Gr-23 in Fig. 4b for peak II is outside of the confidence of prediction of the other data, assuming normal distribution, this data is treated as an outlier. Therefore, sample NMC-Gr-23 is disregarded from the subsequent calculation of thermal triplet of peak II, but not from peak III. In the supplementary materials, all data were included and the thermal triplets were calculated accordingly.

Even though the shape of peak III. indicates a more complex kinetic, its approximation by Arrhenius kinetic may be still feasible if the rate determining process or the decomposition of the main component follows an Arrhenius type kinetic.

Peak I. could not be fitted with the Kissinger plot as it is mentioned previously and the literature values from Refs. [22,23,30] are used for the simulation and listed in Table 5.

The standard errors are calculated by using Eqs. (4) and (5) and are listed in Table 5. In average, the thermal decomposition parameters show 10–20% relative error. In the literature, relative error data is hardly found. Wang et al. [54] reviewed that the total heat of decomposition of the graphite anode can reach $2000 \text{ Jg}^{-1} \pm 300 \text{ Jg}^{-1}$, which shows similar variation to our data. As every electrode coin's composition and also every cell assembly (e.g. pressure applied), may slightly vary, the lithiation, delithiation level of anode and cathode are different. This, in turn, contributes to the uncertainty of DSC measurement results. While higher accuracy may be achieved by optimizing the experimental conditions, this is not the scope of this study. In our following work, sensitivity analysis is used to understand also the effect of uncertainty of measurement results on the overall outcome of TR initiation.

The next step is to build an approximate reaction kinetic model to

Table 5

Determined thermal triplets and standard error (st.err.) of the lithiated anode decomposition reactions.

	Total	Peak I.	Peak II.	Peak III.
h, Heat release Jg^{-1}	–934.08	–1312	–479.397	–208.15
mean (st. err.)	(76.47)	[29]	(63.0)	(2339.4)
E, Activation energy/$\text{J } 10^{-19}$ (st. err.)	–	2.24 [29]	2.69 (0.41)	1.60 (0.57)
A, Frequency factor/s^{-1} (st. err.)	–	$1.67 \cdot 10^{15}$ [29]	$1.78 (0.52) \cdot 10^{14}$	$5.62 (3.16) \cdot 10^6$

describe the heat generation associated to the decomposition of lithiated graphite during TR.

As shown previously, the reactions in region 2 and region 3 are different. Therefore, neither Richard's [29] nor Feng's model [20] has been chosen, but the double breakdown mechanism suggested by Refs. [14,24,35]. The p -SEI does not break down, but transforms to more stable compounds or a thicker layer (reaction 5 in Table 1) called secondary SEI (s-SEI), which compensates the enhanced reactivity between the more mobile Li and EC at elevated temperature.

Since peak I. in region 2 could not be fitted by the Kissinger analysis, a diffusion type kinetic, as suggested by Richard et al. [29], is used

$$\frac{dx_{LiC}}{dt} = -A_{LiC}x_{LiC} \exp\left(-\frac{E_{LiC}}{k_B T}\right) \exp\left(-\frac{t_{SEI}}{t_{SEI,Ref}}\right) \quad 6$$

$$\frac{dt_{SEI}}{dt} = A_{LiC}x_{LiC} \exp\left(-\frac{E_{LiC}}{k_B T}\right) \exp\left(-\frac{t_{SEI}}{t_{SEI,Ref}}\right) \quad 7$$

where A_i , E_i , x_i , t_i are the frequency factor (s^{-1}), activation energy (J), dimensionless concentration, thickness of the diffusion layer of SEI ($i = \text{SEI}$) and lithiated graphite ($i = \text{LiC}$) respectively. k_B , T are the Boltzman constant (J K^{-1}) and the temperature of the sample (K), respectively.

The formation of the secondary SEI is supposed to be the rate determining step, so this process governs the dynamics of the DSC curve. The consecutive SEI decomposition, if it happens, is supposed to be a fast Arrhenius type process, which may affect the total heat of the overall reaction, but not the dynamics.

The second breakdown happens in region 3. There are two options to implement the kinetics. It is possible that the secondary SEI breaks down reducing the thickness of SEI (t_{SEI}) in Eq. (7) which in turn facilitates LiC decomposition (Eq. (6)). As the reactions in region 2 and 3 found to be different, the introduction of a new kinetic equation is proposed which accounts for the Li-EC reaction and also for the secondary SEI decomposition according to reactions 6, 8 and 9 in Table 1. Peak II. in region 3 could be fitted with an Arrhenius type kinetic, but it is probably a mixed reaction. At the moment, the DSC measurement results do not support a reliable separation between the secondary SEI breakdown and the Li-EC reaction in region 3. As reactions 8 and 9 in Table 1 both consume intercalated Li, the proposed kinetic equation modifies Eq. (6) as follows

$$\frac{dx_{LiC}}{dt} = -A_{Li-EC}x_{LiC} \exp\left(-\frac{E_{Li-EC}}{k_B T}\right) - A_{LiC}x_{LiC} \exp\left(-\frac{E_{LiC}}{k_B T}\right) \exp\left(-\frac{t_{SEI}}{t_{SEI,Ref}}\right) \quad 8$$

where A_{Li-EC} , E_{Li-EC} , x_{LiC} are the frequency factor (s^{-1}), activation energy (J), dimensionless concentration of the LiC (according to the reaction scheme #8,9 in Table 1). In a more realistic description, EC consumption should be taken into account, also because Eqs. (6)–(8) consume both, intercalated Li and EC. In the current model, it is supposed that EC is abundantly present during the reaction, its actual concentration is not included into Eq. (8).

In region 4, despite the complex nature of the processes, an Arrhe-

nius type single component decomposition is proposed to approximate the system behaviour:

$$\frac{dx_B}{dt} = -A_B x_B \exp\left(-\frac{E_B}{k_B T}\right) \quad (9)$$

where A_B , E_B , x_B are the frequency factor (s^{-1}), activation energy (J), dimensionless concentration of binder and other reaction components from the previous decomposition processes in other regions.

All the generated heat is assumed to be released, therefore the temperature of the samples is calculated from the constant heating rate

$$\frac{dT}{dt} = a \quad (10)$$

where a is the heating rate ($K s^{-1}$). Then the differential equation system Eqs. (7)–(10) is solved resulting in the dimensionless concentration-time functions. The heat flow ($mWmg^{-1}$) is calculated by the following sum separately for the anode and cathode.

$$\frac{dQ}{dt} = \sum_i \frac{dx_i}{dt} h_i \quad (11a)$$

h_i is the specific reaction heat (Jg^{-1}), x_i is the dimensionless concentration and i is the number of decomposition reactions (Eqs. (6)–(9)).

Fig. 5a compares simulated heat release - shown at $10^\circ C min^{-1}$ - but prevail for all other heating rates - for the single break-down mechanism and the proposed double breakdown mechanism. The single break down mechanism (blue curve) was calculated using data from Refs. [22,23,30]. In the original work of Richard [23,29], it was stated that the model is more suitable to capture the on-set temperature and that for the simulation of TR, further processes need to be incorporated into the model. In their model, the diffusion layer continuously thickens by slowing down the decomposition reaction of graphite, which in turn, results in a broad peak ending well above $500^\circ C$ such as it is shown in Fig. 5a. In our system (Fig. 3), however the heat generation ends around $350^\circ C$, therefore the introduction of a double break down procedure fits better to the experimental data. The blue curve in Fig. 5b shows the simulated dimensionless concentration of intercalated Li. It starts to decrease after the first breakdown but slows down as the secondary SEI forms simultaneously. The change in the slope at ca. $220^\circ C$ corresponds to the transition from diffusion-type to Arrhenius type reaction as the second breakdown of the SEI layer kicks in. The orange curve, in Fig. 5b, illustrates the simulated binder and s-SEI components consumption, as proposed in Eq. (9).

Even though the proposed approximation does not reproduce all features of the DSC curve, it enables a suitable prediction of the heat

generation for this specific system. Further generalization, e.g. to other initial lithiation states, active materials, electrolytes and binder, requires further studies, though.

In supplementary materials, Fig. S2a shows the comparison of heat flow when the outlier (NMC-Gr-23) was taken into account, which only creates higher standard error with more overlap of simulated peaks. However, it does not modify the simulated heat flow considerably.

3.3. Decomposition of NMC (111) cathode

A similar approach, used in the anode study, is employed for the cathode part: reaction mechanisms identification, followed by thermal analysis of important DSC peaks, calculation of thermal parameters and simulation of heat flow signals.

Fig. 6 shows heat flow ($mWmg^{-1}$), mass loss (wt%), and the relative FTIR intensity of CO_2 ($2346 cm^{-1}$) and EC ($1863 cm^{-1}$) obtained for fully charged NMC(111) cathode active material, as a function of the testing temperature from $5^\circ C$ to $590^\circ C$ at $10^\circ C min^{-1}$ heating rate. An obvious observation is that the generated heat and the heat flow are smaller than that of the anode, which suggests that heat from NMC(111) decomposition is less significant for TR than heat from anode decomposition. A similar pattern of peaks was observed by Fleischhammer et al. [14] for NMC-LMO blend cathode, except the first sharp exothermic peak in region 3. This difference is discussed later.

The decomposition profile of delithiated NMC (Fig. 6) can be split

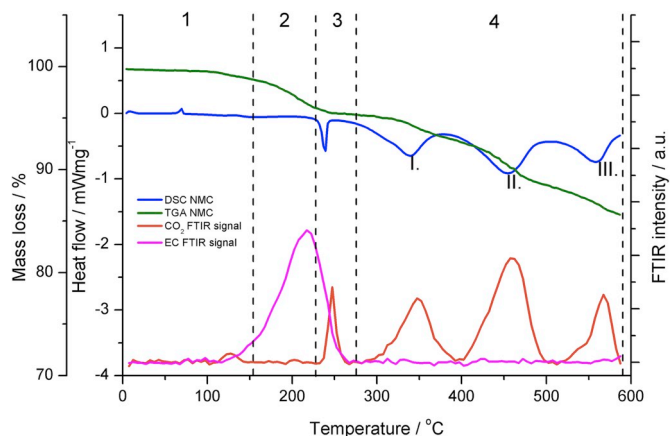


Fig. 6. Simultaneous thermal analysis of de-lithiated NMC(111) cathode at $10 Kmin^{-1}$ of sample#5.

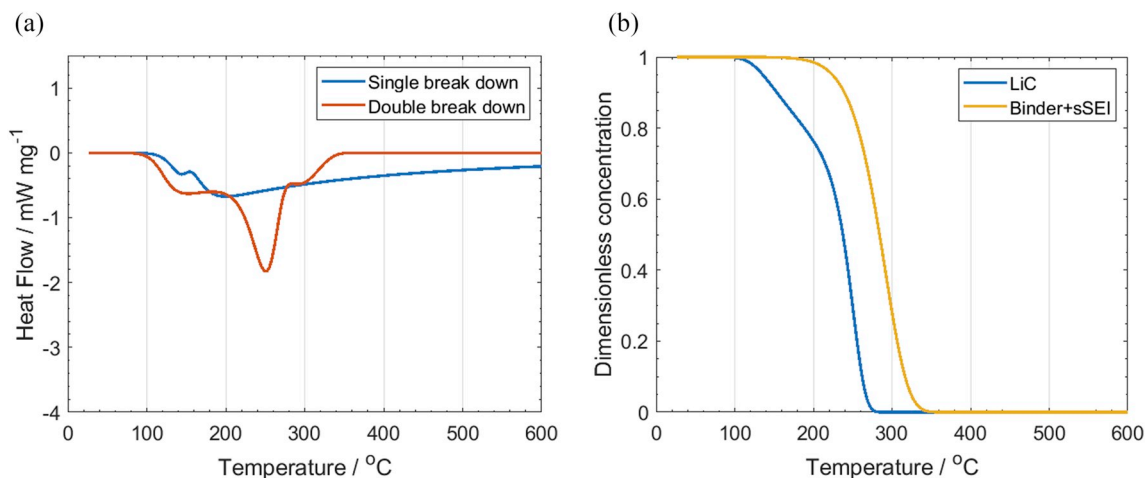


Fig. 5. Simulated heat flow at $10^\circ C min^{-1}$ (as can be measured by DSC) of single and the proposed double break-down mechanism of the anode decomposition (a) and the variation of dimensionless concentration of intercalated Lithium (LiC) and binder together with the secondary SEI (Binder + sSEI) at $10^\circ C min^{-1}$.

into four regions (marked by Arabic numbers). As in the case of the analysis of anode decomposition, not all peaks are taken into account. Roman numbers marks the most significant ones.

In region 1, the peak at ca. 70 °C may have the same origin as described in the anode region 1. Later, CO₂ increase without significant heat release is also visible a bit above 100 °C, similar to the behavior of graphite in the same temperature range (CO₂ intensity curve in Fig. 3). It might have the same reason that the evaporation of traces of water from the pores reacts with organic compounds or LiPF₆ resulting in CO₂ generation. As for the anode, this endothermic peak is neglected from further analysis and calculations.

In region 2 in Fig. 6, an increase of EC characteristics FTIR signal accompanied with mass loss and a small endothermic heat flow are visible around 200 °C. Consequently, this small endothermic signal is associated with EC evaporation. The endothermic heat is more pronounced for heating rate 15 K min⁻¹ in Fig. 7a. This endothermic peak overlaps with other exothermic process, therefore it is hard to analyse by Kissinger analysis and a different approach is applied in this work.

In region 3, a sharp exothermic peak and simultaneous jump in CO₂ and drop of EC are shown in Fig. 6 between 240 °C and 290 °C. The following options can describe the observed heat generation, mass loss and gaseous compounds:

1. Reaction of HF from the decomposed LiPF₆ with NMC according to reaction 15 in Table 2
2. Electrolyte decomposition or the reaction of EC with LiPF₆ (PF₅) according to reaction 20, 19 in Table 3, respectively

3. Burning of EC with the released O₂ from NMC decomposition. The temperature range also matches the first O₂ liberation found by Li et al. [39]
4. Autocatalytic decomposition of NMC similar to LCO decomposition suggested by Refs. [22,23,30]

Reaction 15 generates H₂O, which was not found and does not generate CO₂, therefore option 1 is not considered as the main reaction. Options 2–4 can be hard to separate therefore, they are all taken into account and the possible governing reaction is analyzed by simulation later.

In region 4, three exothermic peaks can be found. The decomposition of NMC accelerates with temperature, resulting in more generated oxygen. The oxygen may further react with the carbon additive resulting in CO₂ generation, as suggested by the increased CO₂ FTIR signal in Fig. 6. Most probably, the heat generated in this region results from simultaneous NMC decomposition and burning of carbon additive. We may suppose that burning of carbon is faster than NMC decomposition, therefore the thermal parameters (e.g. frequency factor etc.) are characteristic to the NMC decomposition and oxygen liberation. Above 350 °C, heat generation slows down which corresponds with the finding by Li et al. [39] that physically absorbed oxygen should be released from NMC(111) below 350 °C.

In the temperature range of 400–500 °C, Li et al. [39] did not find major oxygen release, in contrast to DSC and CO₂ peaks (peak II.) found in Fig. 6. However, this temperature range is where the NMC binder decomposes (Fig. S1c in supplementary materials). The active material's weight loss in this temperature range varies between 2.97 and 3.54 wt%, which matches the expected weight loss associated with PVDF

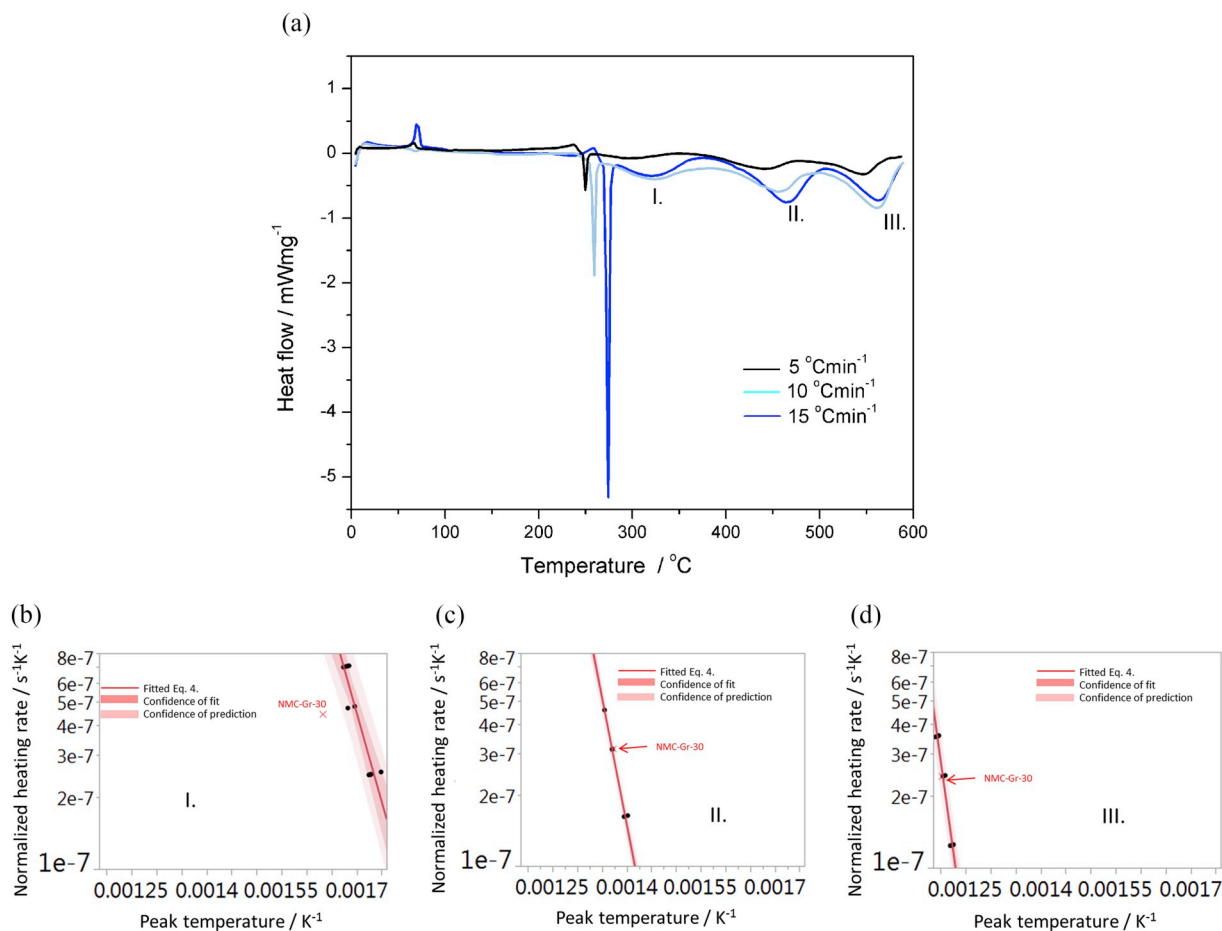


Fig. 7. Heat flow of de-lithiated cathode at heating rates of 5, 10 and 15 °C min⁻¹ of samples #1, 5, 9(a) and Kissinger plots of peak I. (b), II. (c) and III. (d) for all experiments from Table 4. Consequently, the following kinetic expressions are suggested in region 3.

decomposition (the calculation is in supplementary materials). Therefore, peak II is attributed to the decomposition of the PVDF binder.

Peak III. is in the temperature range 500–600 °C and follows the predicted release of chemically bound oxygen found by Li et al. [39]. The same can be concluded as for peak I, i.e. the liberated oxygen burns the carbon or other organic compounds.

In spite of the decomposition probably follows a more complex kinetics, the shift of the peaks with increasing heating rate is clearly visible in Fig. 7a. The thermal triplets of NMC peak I-III are calculated by the Kissinger analysis. The Kissinger plot of peak I. is shown in Fig. 7b. Data of sample NMC-Gr-30 is identified as an outlier, because it is outside of the confidence of prediction band of the other data, and it is therefore excluded from the analysis. However, in supplementary materials, the thermal data is also calculated by taking into account all samples for comparison purposes. The latter case shows similar results, but with more overlapping heat flow peaks (Fig. S2b in supplementary materials). The Kissinger analysis of peak II-III in Fig. 7c and d shows a good fit on all data. The calculated thermal parameters and their relative error (without the outlier) are listed in Table 6, assuming normal distribution of error.

The thermal parameters of the simultaneous processes of evaporation, decomposition and combustion of EC in region 2 and 3 are approximated differently (i.e. not by Kissinger analysis). The thermal parameters of EC decomposition are taken from Peng et al. [55,56]. The combustion of EC is approximated by data from Ref. [57] and fire calorimetry data assuming an average heat of the combustion of organic materials, which is usually used in other studies [58]. The activation energy and the frequency factor of EC evaporation is determined from the differentiation of the mass loss (DTG) in time. Since no reaction between EC and NMC is assumed, the mass loss is supposed to be governed by only EC evaporation. Therefore, the maximum peak temperatures of the DTG signals at different heating rates are able to be analyzed by Kissinger's method (Fig. S3 in supplementary materials). The evaporation heat of EC is taken from the NIST database. In Table 7, the mean value of kinetic parameters are listed for EC evaporation, decomposition and combustion.

The decomposition of NMC:

$$\frac{dx_{NMC-I}}{dt} = -A_{NMC-I} x_{NMC-I} \exp\left(-\frac{E_{NMC-I}}{k_B T}\right) \quad 11b$$

Liberation of oxygen:

$$\frac{dx_{O_2}}{dt} = y_{O_2} A_{NMC-I} x_{NMC-I} \exp\left(-\frac{E_{NMC-I}}{k_B T}\right) \quad 12$$

Consumption of electrolyte by decomposition, evaporation and combustion:

$$\begin{aligned} \frac{dx_{EL}}{dt} = & -A_{EL} x_{EL} \exp\left(-\frac{E_{EL}}{k_B T}\right) - A_{EVA} x_{EL} \exp\left(-\frac{E_{EVA}}{k_B T}\right) \\ & - A_{COM} x_{EL} x_{O_2} \exp\left(-\frac{E_{COM}}{k_B T}\right) \end{aligned} \quad 13$$

Region 4 is calculated by the decomposition of binder (peak II.) and the further decomposition of NMC (peak III.):

Table 6

Determined thermal triplets and standard error (st.err.) of the de-lithiated NMC (111) decomposition reactions.

	Total	Peak I.	Peak II.	Peak III.
<i>h</i> , Heat release (st. err.)/Jg ⁻¹	-553.05 (55.81)	-100.02 (17.43)	-212.90 (19.29)	-189.02 (17.49)
<i>E</i> , Activation energy (st.err.)/J 10 ⁻¹⁹	-	2.35 (0.30)	3.41 (0.13)	4.80 (0.40)
<i>A</i> , Frequency factor (st.err.)/s ⁻¹	-	3.22 (0.93) 10 ¹⁰	3.78 (0.30) 10 ¹²	1.30 (0.20) 10 ¹⁶

Table 7

Kinetic constants of EC evaporation, decomposition and combustion. The evaporation of EC is measured in this work and the calculated data and the standard error in bracket are given. The combustion is estimated from Refs. [57, 58] and the decomposition data is based on literature values [55].

	Evaporation	Combustion	Decomposition
<i>h</i> , Heat release Jg ⁻¹	625 (NIST)	-20 000	-155
<i>E</i> , Activation energy/J 10 ⁻¹⁹	1.58 (0.16)	2.1	37.8
<i>A</i> , Frequency factor/s ⁻¹	2.23 (0.7) 10 ⁷	5.14 10 ¹⁸	5.14 10 ²⁵

$$\frac{dx_{NMC-II}}{dt} = -A_{NMC-II} x_{NMC-II} \exp\left(-\frac{E_{NMC-II}}{k_B T}\right) \quad 14$$

$$\frac{dx_{NMC-III}}{dt} = -A_{NMC-III} x_{NMC-III} \exp\left(-\frac{E_{NMC-III}}{k_B T}\right) \quad 15$$

where *A_i*, *E_i*, *x_i* are the frequency factor (s⁻¹), activation energy (J), dimensionless concentration, of *i* = NMC_I, NMC_II, NMC_III, EL, EVA, COM are peak I-III, electrolyte decomposition, EC evaporation EC combustion, respectively. *k_B*, *T* are the Boltzman constant (J K⁻¹) and the temperature of the sample (K), respectively.

In spite of the fact that oxygen release is expected in Eq. (15), it is considered to react immediately with the carbon additive to form CO₂ (reaction 14, Table 2). Therefore, it is subsumed in Eq. (14)-(15) and not calculated separately to save computational time and preserve the stability of the model.

The simulated heat flow is shown in Fig. 8a (parameters are taken from Tables 6 and 7). When electrolyte is added and both combustion and evaporation are considered, the simulation result matches the measured DSC curves in Fig. 6. Nevertheless, when EC combustion is not considered, the simulated DSC curve is closer to the experimental results of Fleischhammer et al. [14]. They did not find a sharp exothermic peak around 250–290 °C in their DSC study on LMO/NMC blend cathode, however the other identified peaks match with our findings. The absence of the sharp peak might be related to the manually pierced crucible, used in Ref. [14], which had a bigger hole compared to our laser pierced crucible with 5 μm hole. The larger opening might have led to fast release of EC and O₂ from the system and their mixture did not reach the flash point. Consequently, the sharp exothermic peak is not related with the autocatalytic decomposition of NMC but the combustion of electrolyte with the liberated oxygen from NMC.

The simulated heat flow of the cathode decomposition is shown in Fig. 8a at a heating rate of 10 Kmin⁻¹, but this model prevails for all other applied heating rates as it can be seen in supplementary materials (Fig. S4). The dimensionless concentrations are shown in Fig. 8b. The evaporated and the combusted EC are shown as negative concentration for the sake of better visibility. First, the EC starts to evaporate which results in a small endothermic heat in Fig. 8a and a drop in concentration of EC (EC, purple line) in Fig. 8b. Then the NMC-I decomposes and the physically adsorbed oxygen is released (O₂). The oxygen concentration does not increase simultaneously with NMC-I decomposition because it immediately reacts with EC generating the sharp exothermic peak (Fig. 8a). When EC evaporated, the sharp exothermic peak ends abruptly. Later, oxygen concentration (O₂ green line) increases in the simulation. In reality, O₂ does not accumulate, but reacts most probably with the carbon additive immediately. In the current stage of model development, however it is not taken into account separately because carbon combustion heat is considered in the reaction heat of Eq. (14)-(15).

EC decomposition in this system does not happen because EC evaporates faster.

4. Conclusion

For modelling thermal runaway of Graphite – NMC (111) lithium-ion batteries, the thermal decomposition reactions and their parameters

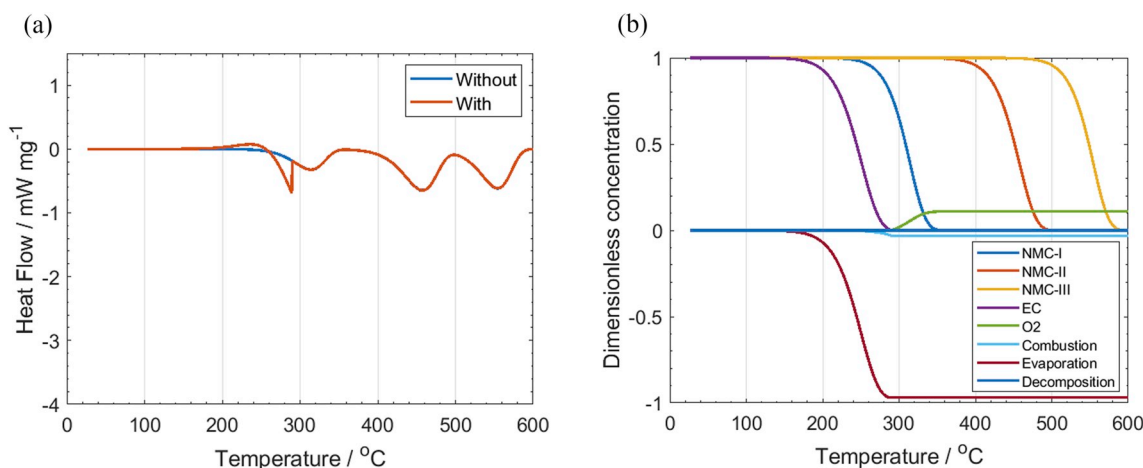


Fig. 8. Simulated heat flow (as it can be measured by DSC) of the NMC(111) decomposition and its reaction with and without electrolyte at 10 Kmin⁻¹ (a) and the dimensionless concentrations when EC reactions are considered (b). Evaporation, decomposition and combustion of electrolyte are plotted in the negative segment and their sum is equal to the decrease of EC.

were measured and determined using Simultaneous Thermal Analysis (STA) coupled with gas analysis.

DSC for both the anode and cathode decomposition showed that multiple reactions occur between 5 and 600 °C. In this work, all major heat sources (or sinks) were identified and their kinetics estimated. The thermal properties (reaction heat, frequency factor, activation energy) of each process and their standard error were determined.

A double break down mechanism is proposed for describing decomposition of the anode. The simultaneous DSC, TGA and gas analysis showed that the primary SEI does not decompose fully in a single step, but with simultaneous formation of a secondary SEI layer. These reactions are modelled by diffusion type decomposition and formation mechanisms. Later a second breakdown occurs, decomposing the secondary SEI and consuming the intercalated Li. Meanwhile, the EC evaporates and decomposes simultaneously. In a third process, the more stable decomposition products and the binder decompose.

During the decomposition of cathode, the following sub-processes were identified and are modelled: evaporation of EC, decomposition of NMC with liberation of oxygen, combustion of EC with the liberated oxygen, decomposition of binder, decomposition of EC and combustion of carbon additive.

The simulated heat flow based on the experimentally deduced thermal parameters shows a good agreement with the STA signals in a broad temperature range. It can also be assumed that there is a coupling between the different processes, which may considerably alter the outcome of the simulated thermal runaway under different conditions.

In the follow up paper, thermal runaway will be modelled with a broad range of thermal parameter combinations, derived from the measurement's uncertainty estimated here.

Acknowledgements

Authors thank Marc Steen for his excellent support reviewing this manuscript.

Appendix A. Supplementary data

Supplementary data to this article can be found online at <https://doi.org/10.1016/j.jpowsour.2019.226774>.

References

- [1] V. Ruiz, A. Pfrang, A. Kriston, N. Omar, P. Van den Bossche, L. Boon-Brett, A review of international abuse testing standards and regulations for lithium ion batteries in electric and hybrid electric vehicles, *Renew. Sustain. Energy Rev.* (2017), <https://doi.org/10.1016/j.rser.2017.05.195>.
- [2] A. Pfrang, A. Kriston, V. Ruiz, N. Lebedeva, F. di Persio, Safety of Rechargeable Energy Storage Systems with a Focus on Li-Ion Technology, 2017, <https://doi.org/10.1016/B978-0-323-42977-1.00008-X>.
- [3] Office of Aviation Safety, Interim Factual Report, Boeing 787-8, JA829J, Japan Airlines, NATIONAL TRANSPORTATION SAFETY BOARD, Office of Aviation Safety, Washington, DC, 2013. <https://www.ntsb.gov/investigations/AccidentReports/Reports/DCA13IA037-interim-factual-report.pdf>, 20594.
- [4] Boeing 787 Battery Fire, 2013. <http://www.ntsb.gov/investigations/pages/boeing787.aspx>.
- [5] M. Yoshio, R.J. Brodd, A. Kozawa, Lithium Ion Batteries, Springer, 2015, <https://doi.org/10.1017/CBO9781107415324.004>.
- [6] M. Jacoby, Burning batteries, *Chem. Eng. News* (2007), <https://doi.org/10.1021/cen-v085n051.p026>.
- [7] V. Ruiz, L. Boon-Brett, M. Steen, L. Van den Berghe, Putting Science into Standards: Workshop - Summary & Outcomes. Driving Towards Decarbonisation of Transport: Safety, Performance, Second life and Recycling of Automotive Batteries for e-Vehicles, 2016. https://ec.europa.eu/jrc/sites/jrcsh/files/jrc104285_jrc104285_final_report_psis_2016_pubsy_revision.pdf.
- [8] G.T.R. UN, (Global Technical Regulation) on Electric Vehicle Safety. Phase 1. ECE/TRANS/WP.29/2017/138, 2017. <http://www.unece.org/fileadmin/DAM/trans/doc/2017/wp29/ECE-TRANS-WP29-2017-138e.pdf>.
- [9] ISO 6469-1:2009, Electrically propelled road vehicles, Safety specifications – Part 1: On-board rechargeable energy storage system (RESS), *Energy Storage Syst.* (2009).
- [10] UL 1642, Standard for Lithium Batteries, Underwriters Laboratories Inc, 2007.
- [11] S. Abada, G. Marlair, A. Lecocq, M. Petit, V. Sauvant-Moynot, F. Huet, Safety focused modeling of lithium-ion batteries: a review, *J. Power Sources* 306 (2016) 178–192. <https://doi.org/10.1016/j.jpowsour.2015.11.100>.
- [12] D.D. MacNeil, J.R. Dahn, Test of reaction kinetics using both differential scanning and accelerating rate calorimetry as applied to the reaction of Li x CoO₂ in non-aqueous electrolyte, *J. Phys. Chem. A* 105 (2001) 4430–4439, <https://doi.org/10.1021/jp001187j>.
- [13] Q. Wang, J. Sun, X. Yao, C. Chen, Thermal stability of LiPF₆/EC + DEC electrolyte with charged electrodes for lithium ion batteries, *Thermochim. Acta* 437 (2005) 12–16, <https://doi.org/10.1016/j.tca.2005.06.010>.
- [14] M. Fleischhammer, T. Waldmann, G. Bisle, B.I. Hogg, M. Wohlfahrt-Mehrens, Interaction of cyclic ageing at high-rate and low temperatures and safety in lithium-ion batteries, *J. Power Sources* 274 (2015) 432–439, <https://doi.org/10.1016/j.jpowsour.2014.08.135>.
- [15] E.P. Roth, D.H. Doughty, Thermal abuse performance of high-power 18650 Li-ion cells, *J. Power Sources* 128 (2004) 308–318, <https://doi.org/10.1016/j.jpowsour.2003.09.068>.
- [16] E.P. Roth, D.H. Doughty, J. Franklin, DSC investigation of exothermic reactions occurring at elevated temperatures in lithium-ion anodes containing PVDF-based binders, *J. Power Sources* 134 (2004) 222–234, <https://doi.org/10.1016/j.jpowsour.2004.03.074>.
- [17] H. Yang, X.D. Shen, Dynamic TGA-FTIR studies on the thermal stability of lithium/graphite with electrolyte in lithium-ion cell, *J. Power Sources* 167 (2007) 515–519, <https://doi.org/10.1016/j.jpowsour.2007.02.029>.
- [18] I. Watanabe, J.I. Yamaki, Thermalgravimetry-mass spectrometry studies on the thermal stability of graphite anodes with electrolyte in lithium-ion battery, *J. Power Sources* 153 (2006) 402–404, <https://doi.org/10.1016/j.jpowsour.2005.05.027>.
- [19] G.V. Zhuang, P.N. Ross, Analysis of the chemical composition of the passive film on Li-ion battery anodes using attenuated total reflection infrared spectroscopy, *Electrochem. Solid State Lett.* 6 (2003) A136, <https://doi.org/10.1149/1.1575594>.

- [20] X. Feng, M. Ouyang, X. Liu, L. Lu, Y. Xia, X. He, Thermal runaway mechanism of lithium ion battery for electric vehicles: a review, *Energy Storage Mater.* 10 (2018) 246–267, <https://doi.org/10.1016/j.ensm.2017.05.013>.
- [21] A.W. Golubkov, D. Fuchs, J. Wagner, H. Wiltse, C. Stangl, G. Fauler, G. Voitic, A. Thaler, V. Hacker, Thermal-runaway experiments on consumer Li-ion batteries with metal-oxide and olivin-type cathodes, *RSC Adv.* 4 (2014) 3633–3642, <https://doi.org/10.1039/c3ra45748f>.
- [22] R. Spotnitz, J. Franklin, Abuse behavior of high-power, lithium-ion cells, *J. Power Sources* 113 (2003) 81–100, [https://doi.org/10.1016/S0378-7753\(02\)00488-3](https://doi.org/10.1016/S0378-7753(02)00488-3).
- [23] M.N. Richard, Accelerating rate calorimetry study on the thermal stability of lithium intercalated graphite in electrolyte. II. Modeling the results and predicting differential scanning calorimeter curves, *J. Electrochem. Soc.* 146 (1999) 2078, <https://doi.org/10.1149/1.1391894>.
- [24] Q. Wang, J. Sun, X. Yao, C. Chen, Thermal behavior of lithiated graphite with electrolyte in lithium-ion batteries, *J. Electrochem. Soc.* 153 (2006) A329, <https://doi.org/10.1149/1.2139955>.
- [25] L. Zhao, I. Watanabe, T. Doi, S. Okada, J. Ichi Yamaki, TG-MS analysis of solid electrolyte interphase (SEI) on graphite negative-electrode in lithium-ion batteries, *J. Power Sources* 161 (2006) 1275–1280, <https://doi.org/10.1016/j.jpowsour.2006.05.045>.
- [26] N.S. Choi, I.A. Profatilova, S.S. Kim, E.H. Song, Thermal reactions of lithiated graphite anode in LiPF₆-based electrolyte, *Thermochim. Acta* 480 (2008) 10–14, <https://doi.org/10.1016/j.tca.2008.09.017>.
- [27] B.S. Parimalam, A.D. MacIntosh, R. Kadam, B.L. Lucht, Decomposition reactions of anode solid electrolyte interphase (SEI) components with LiPF₆, *J. Phys. Chem. C* 121 (2017) 22733–22738, <https://doi.org/10.1021/acs.jpcc.7b08433>.
- [28] E. Jakab, E. Mészáros, J. Borsa, Effect of slight chemical modification on the pyrolysis behavior of cellulose fibers, *J. Anal. Appl. Pyrolysis* 87 (2010) 117–123, <https://doi.org/10.1016/j.jaap.2009.10.012>.
- [29] M.N. Richard, J.R. Dahn, Accelerating rate calorimetry study on the thermal stability of lithium intercalated graphite in electrolyte. I. Experimental, *J. Electrochem. Soc.* 146 (1999) 2068–2077, <https://doi.org/10.1149/1.1391893>.
- [30] T.D. Hatchard, D.D. MacNeil, A. Basu, J.R. Dahn, Thermal model of cylindrical and prismatic lithium-ion cells, *J. Electrochem. Soc.* 148 (2001) A755, <https://doi.org/10.1149/1.1377592>.
- [31] G.H. Kim, A. Pesaran, R. Spotnitz, A three-dimensional thermal abuse model for lithium-ion cells, *J. Power Sources* 170 (2007) 476–489, <https://doi.org/10.1016/j.jpowsour.2007.04.018>.
- [32] P.T. Coman, E.C. Darcy, C.T. Veje, R.E. White, Modelling Li-ion cell thermal runaway triggered by an internal short circuit device using an efficiency factor and Arrhenius formulations, *J. Electrochem. Soc.* 164 (2017) A587–A593, <https://doi.org/10.1149/2.0341704jes>.
- [33] X. Feng, J. Sun, M. Ouyang, X. He, L. Lu, X. Han, M. Fang, H. Peng, Characterization of large format lithium ion battery exposed to extremely high temperature, *J. Power Sources* 272 (2014) 457–467, <http://www.scopus.com/inward/record.url?eid=2-s2.0-84907191494&partnerID=40&md5=c3ea08a019fe2f52dca17691c588ba1a>.
- [34] X. Feng, L. Lu, M. Ouyang, J. Li, X. He, A 3D thermal runaway propagation model for a large format lithium ion battery module, *Energy* 115 (2016) 194–208, <https://doi.org/10.1016/j.energy.2016.08.094>.
- [35] J.-I. Yamaki, H. Takatsuji, T. Kawamura, M. Egashira, Thermal stability of graphite anode with electrolyte in lithium-ion cells, *Solid State Ionics* 148 (2002) 241–245, [https://doi.org/10.1016/S0167-2738\(02\)00060-7](https://doi.org/10.1016/S0167-2738(02)00060-7).
- [36] R. Jung, M. Metzger, F. Maglia, C. Stinner, H.A. Gasteiger, Oxygen release and its effect on the cycling stability of LiNi_xMn_yCo_zO₂ (NMC) cathode materials for Li-ion batteries, *J. Electrochem. Soc.* 164 (2017) A1361–A1377, <https://doi.org/10.1149/2.0021707jes>.
- [37] I. Buchberger, S. Seidlmayer, A. Pokharel, M. Piana, J. Hattendorff, P. Kudejova, R. Gilles, H.A. Gasteiger, Aging analysis of graphite/LiNi_{1/3}Mn_{1/3}Co_{1/3}O₂ cells using XRD, PGAA, and AC impedance, *J. Electrochem. Soc.* (2015), <https://doi.org/10.1149/2.0721514jes>.
- [38] P. Peng, F. Jiang, Thermal safety of lithium-ion batteries with various cathode materials: a numerical study, *Int. J. Heat Mass Transf.* 103 (2016) 1008–1016, <https://doi.org/10.1016/j.ijheatmasstransfer.2016.07.088>.
- [39] J. Li, Z.R. Zhang, X.J. Guo, Y. Yang, The studies on structural and thermal properties of delithiated Li_xNi_{1/3}Co_{1/3}Mn_{1/3}O₂ (0 < x ≤ 1) as a cathode material in lithium ion batteries, *Solid State Ionics* 177 (2006) 1509–1516, <https://doi.org/10.1016/j.ssi.2006.03.055>.
- [40] C.L. Campion, W. Li, B.L. Lucht, Thermal decomposition of LiPF₆-based electrolytes for lithium-ion batteries, *J. Electrochem. Soc.* 152 (2005) A2327, <https://doi.org/10.1149/1.2083267>.
- [41] Q.S. Wang, J.H. Sun, G.Q. Chu, X.L. Yao, C.H. Chen, Effect of LiPF₆ on the thermal behaviors of four organic solvents for lithium ion batteries, *J. Therm. Anal. Calorim.* 89 (2007) 245–250, <https://doi.org/10.1007/s10973-006-7534-1>.
- [42] H. Yang, G.V. Zhuang, P.N. Ross, Thermal stability of LiPF₆ salt and Li-ion battery electrolytes containing LiPF₆, *J. Power Sources* 161 (2006) 573–579, <https://doi.org/10.1016/j.jpowsour.2006.03.058>.
- [43] Safety Datasheet DMC, (n.d.). <https://www.alfa.com/en/msds/?language=EE&subformat=CLP1&sku=A13104> (accessed March 28, 2019).
- [44] Safety Datasheet, EC, (n.d.). <https://www.alfa.com/en/msds/?language=EE&subformat=CLP1&sku=A15735> (accessed March 28, 2019).
- [45] C. Daniel, J.O. Besenhard (Eds.), *Handbook of Battery Materials*, Wiley-VCH Verlag GmbH & Co. KGaA, Weinheim, Germany, 2011, <https://doi.org/10.1002/9783527637188>.
- [46] NIST Chemistry Workbook, (n.d.). <https://webbook.nist.gov/chemistry/> (accessed March 28, 2019).
- [47] Z. Chen, Y. Qin, Y. Ren, W. Lu, C. Orendorff, E.P. Roth, K. Amine, Multi-scale study of thermal stability of lithiated graphite, *Energy Environ. Sci.* 4 (2011) 4023–4030, <https://doi.org/10.1039/c1ee01786a>.
- [48] T. Waldmann, B.I. Hogg, M. Wohlfahrt-Mehrens, Li plating as unwanted side reaction in commercial Li-ion cells – a review, *J. Power Sources* 384 (2018), <https://doi.org/10.1016/j.jpowsour.2018.02.063>.
- [49] T. Waldmann, J.B. Quinn, K. Richter, M. Kasper, A. Tost, A. Klein, M. Wohlfahrt-Mehrens, Electrochemical, post-mortem, and ARC analysis of Li-ion cell safety in second-life applications, *J. Electrochem. Soc.* 164 (2017) A3154–A3162, <https://doi.org/10.1149/2.0961713jes>.
- [50] O. Haik, S. Ganin, G. Gershinsky, E. Zinigrad, B. Markovsky, D. Aurbach, I. Halalay, On the thermal behavior of lithium intercalated graphites, *J. Electrochem. Soc.* 158 (2011) A913, <https://doi.org/10.1149/1.3598173>.
- [51] L. El Ouatani, R. Dedryvère, J.B. Ledeuil, C. Siret, P. Biensan, J. Desbrières, D. Gonbeau, Surface film formation on a carbonaceous electrode: influence of the binder chemistry, *J. Power Sources* 189 (2009) 72–80, <https://doi.org/10.1016/j.jpowsour.2008.11.031>.
- [52] H. Yang, H. Bang, K. Amine, J. Prakash, Investigations of the exothermic reactions of natural graphite anode for Li-ion batteries during thermal runaway, *J. Electrochem. Soc.* 152 (2005) A73, <https://doi.org/10.1149/1.1836126>.
- [53] H.E. Kissinger, Reaction kinetics in differential thermal analysis, *Anal. Chem.* (1957), <https://doi.org/10.1021/ac60131a045>.
- [54] Q. Wang, P. Ping, X. Zhao, G. Chu, J. Sun, C. Chen, Thermal runaway caused fire and explosion of lithium ion battery, *J. Power Sources* 208 (2012) 210–224, <https://doi.org/10.1016/j.jpowsour.2012.02.038>.
- [55] P. Peng, F. Jiang, Thermal behavior analyses of stacked prismatic LiCoO₂ lithium-ion batteries during oven tests, *Int. J. Heat Mass Transf.* 88 (2015) 411–423, <https://doi.org/10.1016/j.ijheatmasstransfer.2015.04.101>.
- [56] X. Feng, X. He, M. Ouyang, L. Lu, P. Wu, C. Kulp, S. Prasser, Thermal runaway propagation model for designing a safer battery pack with 25Ah LiNi_{0.8}CoyMnzO₂ large format lithium ion battery, *Appl. Energy* 154 (2015) 74–91, <https://doi.org/10.1016/j.apenergy.2015.04.118>.
- [57] Y.-Y. Sun, T.-Y. Hsieh, Y.-S. Duh, C.-S. Kao, Thermal behaviors of electrolytes in lithium-ion batteries determined by differential scanning calorimeter, *J. Therm. Anal. Calorim.* 116 (2014) 1175–1179, <https://doi.org/10.1007/s10973-014-3683-9>.
- [58] F. Larsson, J. Anderson, P. Andersson, B.-E. Mellander, Thermal modelling of cell-to-cell fire propagation and cascading thermal runaway failure effects for lithium-ion battery cells and modules using fire walls, *J. Electrochem. Soc.* 163 (2016) A2854–A2865, <https://doi.org/10.1149/2.0131614jes>.